ACS APPLIED MATERIALS & INTERFACES

RESEARCH ARTICLE

www.acsami.org

Microwave-Mediated Synthesis for Improved Morphology and Pseudocapacitance Performance of Nickel Oxide

Sumanta Kumar Meher, P. Justin, and G. Ranga Rao*

Department of Chemistry, Indian Institute of Technology Madras, Chennai-600036, India

Supporting Information

ABSTRACT: Synthetic methods greatly control the structural and functional characteristics of the materials. In this article, porous NiO samples were prepared in conventional-reflux and microwave assisted heating method under homogeneous precipitation conditions. The NiO samples synthesized in conventional reflux method showed flakelike morphology, whereas the sample synthesized in microwave methods showed hierarchical porous ball like surface morphology with uniform ripple-shaped pores. The NiO samples characterized using BET method were found to bear characteristic meso- and macroporosity due to differently crystallized $Ni(OH)_2$ precursors under various heating conditions. Thermogravimety analysis showed morphology dependent decomposition of $Ni(OH)_2$ precursors. The microwave synthesized porous NiO sample with unique morphology and pore size distribution showed significantly improved charge storage and electrochemical stability than the flaky NiO sample synthesized by employing conventional reflux method. The cyclic voltammetry measurements on microwave synthesized NiO sample showed considerably high capacitance and better electrochemical reversibility. The charge−discharge measurements made at a discharge current of 2 A/g showed higher rate specific capacitance (370 F/g) for the NiO sample synthesized by microwave method than the sample synthesized by reflux method (101 F/g). The impedance study illustrates lower electronic and ionic resistance of rippled-shaped porous NiO due to its superior surface properties for enhanced electrode−electrolyte contact during the Faradaic redox reactions. It has been further established from the Ragone plot that the microwave synthesized NiO sample shows higher energy and power densities than the reflux synthesized NiO sample. Broadly, this study reveals that microwave-mediated synthesis approach is significantly a better strategy for the synthesis of porous NiO suitable to electrochemical supercapacitor applications.

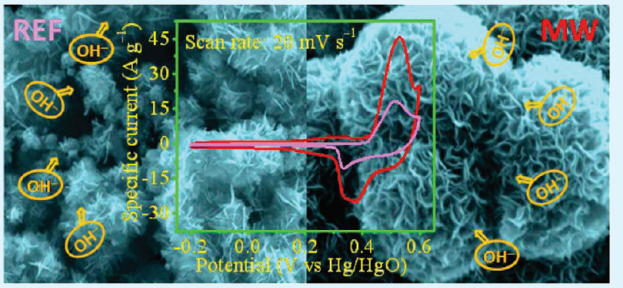

KEYWORDS: microwave-mediated synthesis, conventional reflux method, porous NiO, supercapacitor

1. INTRODUCTION

In the light of recent developments of various efficient energy storage devices, electrochemical supercapacitors are the most investigated systems as they offer higher power and energy density compared to lithium-ion batteries and conventional dielectric capacitors, respectively.[1−6] In addition, supercapacitors also have the advantages of short charging times and longer cycle as well as self-life.[3,7] Therefore, these devices have started playing vital roles as energy buffers and uninterruptable power-sources in electric, hybrid and fuel cell vehicles, memory back-up equipments, cellular phones and entertainment instruments.[4,8] On the basis of the charge storage mechanisms, electrochemical supercapacitors are divided broadly into electrical double layer capacitors (EDLCs) and pseudocapacitors. EDLCs, which bear a typical capacitance value of 10−40 μF cm^{-2}, are based on electrostatic charge separation between electrolyte ions and electrodes whereas pseudocapacitors entail reversible Faradaic redox reactions on the surface of an electro-active material for charge storage, which can have a value of 10−100 times that of EDLCs.[9,10] As surface properties play major role in charge storage mechanism, the most active approach in pseudocapacitor research has been the development of electrode materials with improved surface properties.[11] In materials context, RuO_2 is the mostly studied system with reported specific capacitance value as high as 1580 F g^{-1}.[12] However the toxicity, high cost and narrow operating voltage window of ∼1 V have triggered a search for alternate materials for better technological viability.[13] In this context, many inexpensive transition metal oxides like MnO_2,[14,15] NiO,[16−20] Co_3O_4,[21] MoO_3,[22] V_2O_5[23] and nitrides like TiN[24] have been reported to be highly active as suitable electrode materials. Among these oxides, NiO is a versatile material for supercapaictor applications due to its higher surface area, good redox and charge storage property, controllable size, shape, and structural characteristics.[15−18,25,26] Since the first report of NiO film as active pseudocapacitor material, by Liu and Anderson,[27] numerous attempts have been made to shorten the diffusion path length

Received: March 8, 2011
Accepted: May 13, 2011
Published: May 13, 2011

and increase the ion transfer rate by changing the morphology and other physicochemical properties of NiO material.[16−20] A number of synthetic methods have been developed to prepare NiO as well as NiO-based composites with tunable surface morphologies and characteristic pseudocapacitance behavior.[28−32,20] Some of our recent reports also emphasize the structure−activity relationship of NiO material which accentuates the importance of surface properties on the charge storage performance.[17−19] These studies show that, in addition to the parameters such as surface area and pore size, suitable surface morphology of NiO is also an essential parameter for exhibiting higher pseudocapacitance.

Of late, microwave-mediated synthesis has drawn much attention in organic reactions as well as in the synthesis of oxide materials.[33,34] This is due to the fact that microwave is a nonionizing electromagnetic radiation with higher penetration depth, and greatly enhances the rate of nucleation thereby reducing the time required for synthesis.[35] The microwave treatment does not produce major thermal gradients in the reaction medium and helps in the formation of products with uniform dimensions and high purity.[36] Microwave-mediated synthesis also involves accelerated kinetics that can lead to the formation of particles with uniform dimensions. This is advantageous in controlling the morphology of the material.[33−36] Microwave-mediated synthesis has been adopted successfully to prepare $Ni(OH)_2$ and NiO with uniform microstructures.[37,38] The reported microwave heated syntheses of these materials are mostly hydrothermal mediated where the contribution of hydrothermal condition limits the understanding of microwave effect on the final morphology of the product. Hence it is felt necessary to synthesize NiO samples under nonhydrothermal microwave-reflux conditions to assess the effect of microwave on the evolution of morphology and other properties of the NiO material.

In this study, NiO samples have been synthesized by employing homogeneous precipitation method under microwave-reflux and conventional-reflux conditions. The samples are characterized and their pseudocapacitive behavior has been assessed. The aim is to bring out the physicochemical and pseudocapacitive distinctiveness of NiO sample prepared by nonhydrothermal microwave-reflux method as compared to conventional-reflux method.

2. EXPERIMENTAL SECTION

2.1. Synthesis of NiO Architectures. Analytical grade $Ni(NO_3)_2 \cdot 6H_2O$ (CDH Chemicals), cetyltrimethyl ammonium bromide (CTAB, SD Fine Chemicals), and urea (Thomas-Baker) were used as received. Triply distilled water was used during all the experimental processes. In a typical experiment, 100 mL of aqueous solution of 20 mmol of $Ni(NO_3)_2 \cdot 6H_2O$ was added dropwise to 100 mL of 10 mmol of CTAB, with vigorous stirring, to form a homogeneous solution. Solid urea was added to the resulting solution in the Ni-salt to urea molar ratio of 1:2 and stirred for additional 3 h for complete homogeneity. The resulting solution was then divided in to two equal halves, one half was subjected to refluxing at 120 °C for 12 h, and the other half was treated with microwave irradiation using 250 W power in a CEM Discover Bench Mate microwave reactor at 120 °C for 15 min. The heat treatments resulted in the formation of puffy grass-green solid precipitates. After autocooling the reaction mixtures to room temperature, the products were separated by centrifugation at 3000 rpm, with repeated washing using triple distilled water followed by a mixture of absolute ethanol and water, and finally with absolute ethanol. The materials were then dried in a vacuum oven at 60 °C overnight. The samples were further subjected to calcination in flowing air by heating at the rate of 5 °C min^{-1} from room temperature to 300 °C and maintained for 3 h to obtain the final product. The samples prepared under conventional-reflux and microwave treatments before calcination are denoted as NiO-ref-uc and NiO-mw-uc, respectively, and after calcination as NiO-ref and NiO-mw, respectively.

2.2. Details of Instrumental Analysis. Thermogravimetric analysis of the samples were performed on a TA make TGA Q500 V20.10 Build 36 instrument, in air flow (20 mL per min) and with a linear heating rate of 20 °C per min, from room temperature to 800 °C. The PXRD patterns were obtained using a Bruker AXS D8 Advance diffractometer at room temperature, and at a scan rate of 0.01° s^{-1} using Cu Kα (λ = 0.15408 nm) radiation generated at 40 kV, 30 mA. Multipoint nitrogen adsorption−desorption experiments were carried out by means of an automatic Micromeritics ASAP 2020 analyzer using Brunauer−Emmett−Teller (BET) gas adsorption method at 77 K. The samples were degassed at 100 °C for 2 h followed by 150 °C for 10 h in a dynamic vacuum before physisorption measurements. The specific surface area values were calculated using the software of the instrument based on BET equation. The porosity distribution in the samples were generated from desorption branch of the isotherm using the Barrett−Joyner−Halenda (BJH) method and a cylindrical pore model. Scanning electron microscopy measurements were carried out using a field emission gun equipped FEI Quanta 200 microscope. The sample powders were deposited on carbon tape before mounting on the sample holder for analysis. The high-resolution transmission electron microscopy (HRTEM) measurements were performed on a JEOL 3010 HRTEM with a UHR pole piece operated at an accelerating voltage of 300 kV and a lattice resolution of 0.14 nm.

2.3. Fabrication of Electrodes and Electrochemical Measurements. The working electrodes for evaluating the electrochemical properties of NiO were fabricated by mixing 80 wt % of NiO with 15 wt % acetylene black in an agate mortar. To this mixture, 5 wt % polyvinylidene difluoride (PVdF) binder dissolved in 1-methyl-2-pyrrolidinone (NMP) was added to form slurry. The slurry was coated (area of coating: 1 cm^2) on a pretreated battery-grade polished Ni foil (0.2 mm thick) for electrical conductivity and vacuum-dried at 60 °C for 8 h. Cyclic voltammetry (CV), chronopotentiometry (CP) and electrochemical impedance spectroscopy (EIS) studies were performed using a CHI 7081C electrochemical workstation in a three-electrode configuration with NiO coated Ni plate, Pt foil (1×2 cm^2) and Hg/HgO (1.0 M KOH) as working, counter and reference electrodes, respectively. The measurements were performed using deoxygenated aqueous 1.0 M KOH as the electrolyte. The stability of the materials were evaluated from 1600 galvanostatic charge−discharge test cycles. The electrochemical impedance spectra were measured by imposing a sinusoidal alternating voltage frequency of 1×10^{-2} to 1×10^{5} Hz, alternating current (ac) amplitude of 5 mV and a constant dc bias potential of 0.5 V.

3. RESULTS AND DISCUSSION

The PXRD patterns of NiO-ref-uc and NiO-mw-uc samples shown in Figure 1A represent the characteristic peaks attributable to α and β forms of $Ni(OH)_2$ phases. The NiO-mw-uc sample shows only α-$Ni(OH)_2$ phase whereas NiO-ref-uc sample exhibits peaks corresponding to α-$Ni(OH)_2$ as major phase and β-$Ni(OH)_2$ as minor phase. The measured pH of the reaction medium is about 8.0 to 8.2 which nucleates the formation of α-$Ni(OH)_2$.[18,19] Both uniform heating and accelerated kinetics lead to the formation of single phase product in microwave mediated synthesis.[33−35] However in the case of conventional reflux treatment, the thermal gradient in the reaction medium and longer reaction time induce ripening of some α-$Ni(OH)_2$ phase to β-$Ni(OH)_2$ phase. The formation of $Ni(OH)_2$ precursors in reflux as well as microwave-mediated

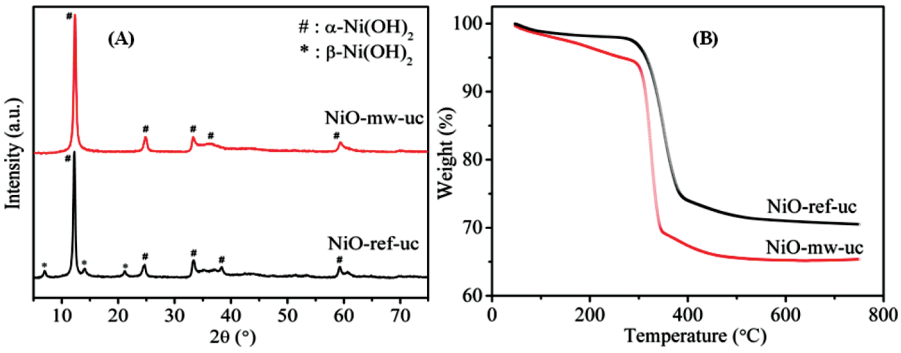

Figure 1. (A) XRD patterns, and (B) TGA profiles of $Ni(OH)_2$ precursor samples synthesized by microwave and reflex methods.

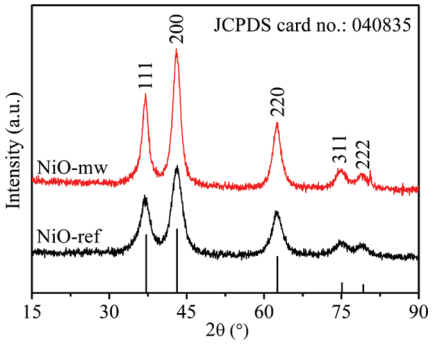

Figure 2. PXRD patterns of NiO-mw and NiO-ref samples. These samples are obtained by calcining NiO-mw-uc and NiO-ref-uc samples (in Figure 1A) at 300 °C in air.

synthesis involves well studied hydrolysis-precipitation process.[17,19,38,39] In this process, slow hydrolysis of urea generates OH^- ion in the reaction medium which further coordinate with Ni^{2+} to form different phases of $Ni(OH)_2$. The OH^- ion generation mostly occurs at a controlled rate which further influences the crystal growth process. The following reactions are involved in the formation of $Ni(OH)_2$[50]

$$NH_2CONH_2 \xrightarrow{\text{hydrolysis}} NH_4^+ + NCO^-$$

$$NCO^- + 3H_2O \rightarrow HCO_3^- + NH_4^+ + OH^-$$

$$Ni^{2+} + 2OH^- \rightarrow Ni(OH)_2$$

Figure 1B shows the TG curves of the NiO-mw-uc and NiO-ref-uc samples. There is significant mass loss observed in both the samples. The first loss has occurred between 40 and 250 °C which corresponds to the elimination of adsorbed and intercalated water. The second mass loss occurs in the range of 250 to 350 °C, with a maximum at 300 °C, which corresponds to the decomposition of $Ni(OH)_2$, ($Ni(OH)_2 \rightarrow NiO + H_2O$), as well as the removal of nitrate and carbonate species.[16−19,38] Further, there is no major weight loss observed at higher temperatures, which indicates the absence of additional phase or structural changes. The weight losses are significantly different in the two regions which correspond to the difference in the amount of adsorbed, intercalated and crystalline water in the samples. Because of structural and morphological differences in the $Ni(OH)_2$ samples, the water content is expected to

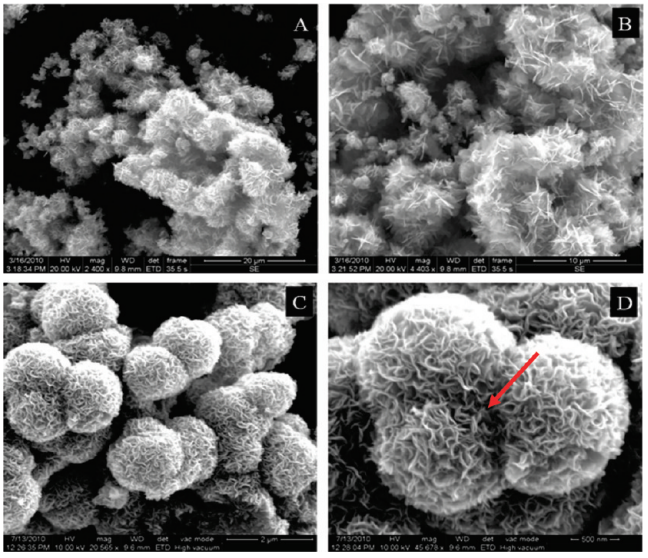

Figure 3. (A) Low- and (B) high-resolution FESEM images of NiO-ref sample. (C) Low and (D) high-resolution FESEM images of NiO-mw sample.

be different. This is reflected in the TGA curves (Figure 1B) in which the total weight loss up to 350 °C is 32% for the NiO-mw-uc sample as compared to 26% for the NiO-ref-uc sample. The difference in weight loss also indicates the variations in structure and crystallinity of the precursor samples that undergo decomposition via two different mechanisms.[16]

The wide-angle PXRD profiles of calcined NiO-mw and NiO-ref samples are shown in Figure 2. The XRD patterns exhibit standard peaks at 2θ values of 37, 43, 62.5, 74.8, and 78.9 degrees assigned respectively to (111), (200), (220), (311), and (110) planes of FCC type NiO with a space group of $Fm\bar{3}m(225)$. Absence of secondary peaks in the PXRD patterns illustrates the stoichiometric purity of the NiO samples. The difference seen in the broadness and intensity of the respective peaks of NiO-mw and NiO-ref samples are attributed to different crystallinity and crystallite size. The XRD peaks of NiO-mw sample are more intense and sharp compared to those of NiO-ref sample. This indicates that the NiO-mw sample is more crystalline than NiO-ref sample. The calculated average crystallite sizes of NiO-mw and NiO-ref samples using Scherrer equation are 4.9 and 3.5 nm, respectively.

The uniform heating, superheating, and accelerated kinetics during the microwave-mediated synthesis results in enhanced crystal growth and better crystallinity of the uncalcined precursor which is translated to the NiO-mw product. The FESEM images the NiO samples are shown in Figure 3. The NiO-ref sample (Figure 3A,B) shows agglomerated flower like regular structures congregated on randomly arranged nanosize flakes. Further insight into the surface structures of aggregated nanoflowers has been obtained by HRTEM analysis. The HRTEM micrographs are presented in Figure 4, which clearly shows random aggregation of nanoflakes forming flower-like surface morphology. On the other hand, the NiO-mw sample (Figure 3C,D) clearly shows highly uniform porous-ball-like structure with rippled-shaped pores. Interestingly, two to three porous balls are found to be aggregated regularly to form complex structures of NiO. The cause of the aggregation seems to be the effect of microwave, which creates "hot surface" on the initially formed NiO porous balls.[40] The "hot surfaces" induce mass transport and directional fusion of porous balls to form arranged superstructures. The absence of such superheating in the conventional-reflux method leads to NiO product without any specific crystallographic and morphological arrangement. The FESEM micrographs also show the porous nature of NiO samples, which is further studied by BET analysis.

To demonstrate the formation mechanism of the NiO samples, the surface morphology of the $Ni(OH)_2$ samples (both NiO-mw-uc and NiO-ref-uc) are analyzed using FESEM and the images are given in Figure S1 of the Supporting Information. The uncalcined samples also show similar morphologies like their calcined counterparts but with noticeably less porosity. It is therefore concluded that the morphologies of both samples are nearly retained during the thermal decomposition of $Ni(OH)_2$ to NiO, and there is significant pore opening observed in the FESEM images of respective NiO samples (Figure 3). As expected, the surface area and porosity of the NiO samples are significantly higher than their respective $Ni(OH)_2$ precursors. The exact formation mechanism of complex mesoporous structures of NiO reported in this paper, and also numerous such structures reported elsewhere in the literature, has not been understood clearly due to various parameters such as hydrophobic interactions, hydrogen bonding, van der Walls forces, crystal-face attraction, electrostatic and dipolar fields, intrinsic crystal contraction, and Ostwald ripening contributing simultaneously during the product formation.[41] In the presence of additives like CTAB, the situation becomes more complicated. This is in agreement with the earlier studies, which show that the extrinsic modulation of crystal growths occurs by selective adsorption of solvents, inorganic additives and surfactants to certain crystallographic planes modifying the relative order of the surface energies.[42−44] The selective adsorption controls the growth of certain crystal planes leading to particular morphology of the material.[17−19] A number of in situ studies combined with theoretical modeling show that the nucleation and growth occurs via aggregation based mechanism to generate crystals with hierarchical structures and complex morphologies.[45] Specifically, the crystal growth seems to proceed via aggregation of nascent precursor units rather than by classical ion by ion mechanism.[46] Similar aggregation type mechanism can also explain the formation of $Ni(OH)_2$ and NiO flowerlike and rippled surface superstructures in this study. Due to the slow and continuous reaction process under homogeneous precipitation conditions, the nascent nickel hydroxide nuclei begin to impinge on the neighboring

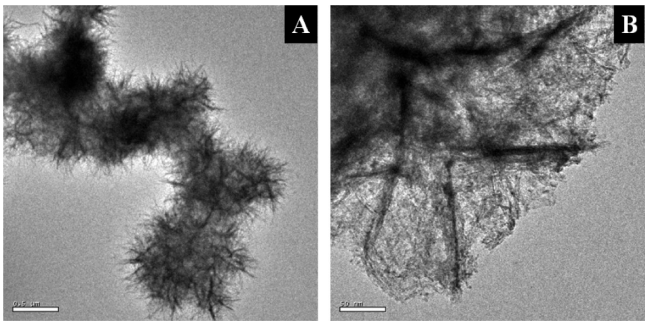

Figure 4. (A) Low- and (B) high-resolution HRTEM images of NiO-ref sample showing flower like morphology, a congregation of randomly arranged nanosize flakes.

crystals and assemble along a particular crystal orientation. The extrinsic crystal growth is modulated to some extent by adsorption of surface energy modifiers like H_2O and anions on certain crystallographic planes. The CTAB surfactant during the synthesis plays a major role in preventing the random agglomeration of the primarily formed crystallites by effectively shielding the OH^- activity further on the nascent crystallites. Since the initially formed $Ni(OH)_2$ crystallites and their growth determine the final morphology, the nature of heat treatment on the final morphology is quite immense. In reflux method, both under the conventional-heating as well as microwave-heating process, the formation of nascent thin flakes of $Ni(OH)_2$ is the result of primary crystallization process. Under conventional-heating conditions, the thin flakes undergo coalescence followed by Ostwald ripening to larger uniform crystals, which self-assemble randomly to transform into flower like morphology.[44] The flowerlike precursor is finally decomposed using heat treatment to produce NiO with high degree of morphological retention. However during the microwave-mediated synthesis, the bulk temperature effects are completely different as compared to the conventional-heating which is caused by the unique microwave dielectric heating mechanism.[33,35] Therefore, microwave radiation not only accelerates the nucleation but also enhances the crystal growth process, and generates higher population of $Ni(OH)_2$ nuclei than the samples nucleated by conventional-heating. This happens mainly because of the higher heating rate which increases the reaction rates by creating hot spots during the reaction. These factors induce the formation of more crystalline $Ni(OH)_2$ than the conventionally synthesized sample. Due to localized heating phenomena in microwave-mediated synthesis, the initially formed nascent $Ni(OH)_2$ flakes undergo rapid growth in size/dimensionality during the coalescence process. During this process, microwave also causes etching of the coalesced nanoflakes to provide a type of rippled surface to the flakes.[47] The rippled flakes then undergo self-assembly induced by the microwave created localized "hot surface" and get fabricated into ball-like structure of lower surface energy with hierarchical porosity. These hierarchical porous balls further undergo "hot surface" induced self-aggregation to give the final morphology. In the case of conventional heating process, the nonexistence of hot surface results in random arrangement of coalesced nanoflakes to give flower-like morphology. The plausible formation mechanisms presented here also gain support from the recent work where time dependent product analysis has been attempted to establish the mechanism.[20,40] The schematic representations of the plausible

Scheme 1. Plausible Mechanisms for the Formation of (A) NiO-ref and (B) NiO-mw Samples

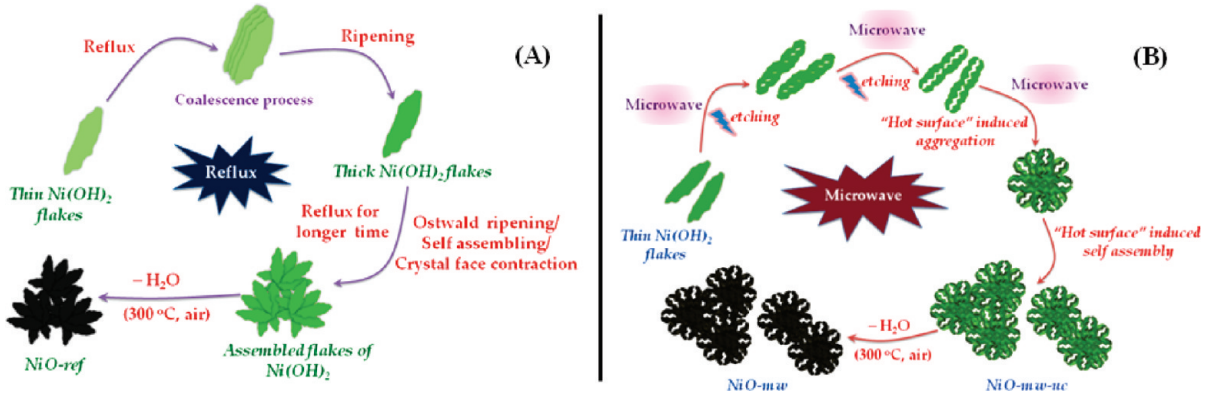

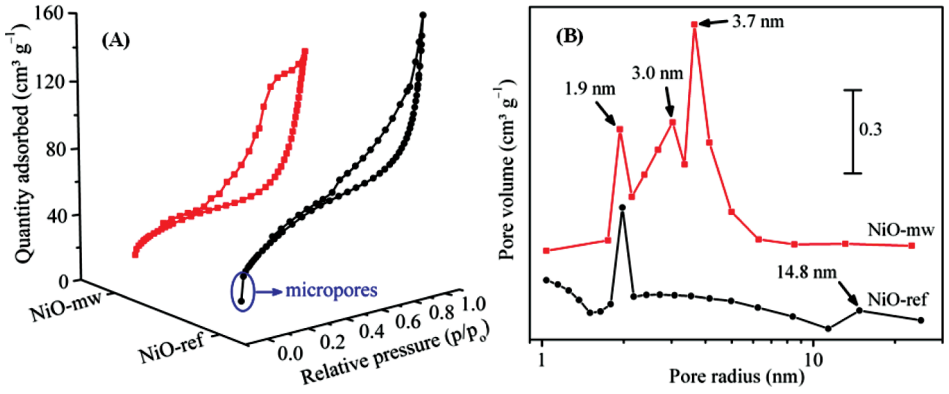

Figure 5. (A) BET isotherms and (B) BJH pore size distribution profiles of NiO-mw and NiO-ref samples.

formation mechanisms of NiO with flower and rippled surface porous ball-like morphologies are presented in Scheme 1.

The greater role of CTAB in the development of specific morphology has been further investigated through comparative synthetic experiments in the absence of CTAB which show that the as-synthesized products exhibit lesser porosity and no particular morphology. In this context, recent report by Zheng et al.,[48] also illustrates that NiO prepared in similar homogeneous precipitation method without using CTAB shows very low surface area and no specific surface morphology.

Nitrogen adsorption−desorption isotherms and BJH pore size distribution plots of the NiO-mw and NiO-ref samples are shown in panels A and B in Figure 5, respectively. The isotherm of NiO-mw sample shows H2 type hysteresis loop which exhibits the presence of network of pores of different sizes.[49] This is well demonstrated in the pore size distribution plot in Figure 5B, where three well distinguished maxima can be observed. It is known that, apart from the surface morphology, factors like interparticle spacing and internal voids also contribute to the characteristic pore size distribution of a material.[40,50] Therefore, the ripple-shaped porous network and the random attachment of porous balls are the apparent reason for the multimodal pore size distribution of the NiO-mw sample. For NiO-ref sample, an isotherm with H2 type hysteresis loop is observed, which is the most common for platelike particles with slit-shaped pores.[49] This observation is well-corroborated with the clear flakelike surface morphology of the NiO-ref sample. The randomly arranged nanoflake structures of NiO-ref sample produce flowery structure with characteristics bimodal pore size distribution as shown in Figure 5B. The pore size distribution maxima of NiO-mw sample are centered at ∼1.9, 3.0, and 3.7 nm, which are most suited for better OH^- diffusion in electrochemical supercapacitor application. However, the observed pore size distribution of NiO-ref sample centered at ∼1.8 and 14.9 nm does not provide feasible accessibility to OH^- for efficient/sufficient redox reactions in electrochemical energy storage applications.[6] The higher adsorption in NiO-ref sample at p/p_0 = 0.9−1.0 observed in Figure 5A is the clear evidence of presence of higher fraction of macropores, as compared to NiO-mw sample. The BET specific surface area and the corresponding pore volume of the NiO-mw and NiO-ref samples, respectively, are 125 and 167 m^2/g, and 0.22 and 0.23 cm^3/g. It is to be noted that the NiO-mw sample that loses the greater amount of water in TGA is expected to show higher surface area than the NiO-ref sample. However, the micropores generated during the thermal decomposition are responsible for the rapid adsorption at p/p_0 = 0−0.02 and better BET specific surface area and pore volume of NiO-ref sample.[16]

From the BET surface area and pore size analysis, it can be stated that the NiO samples with flowerlike and rippled surface ball-like morphology show hierarchical porosity that generally corresponds to the pore volume distribution within a material because of the range of pores of different sizes. The hierarchical porosity is significant, particularly for surface selectivity of molecules with specific sizes. Simon and Gogotsi[6] have recently

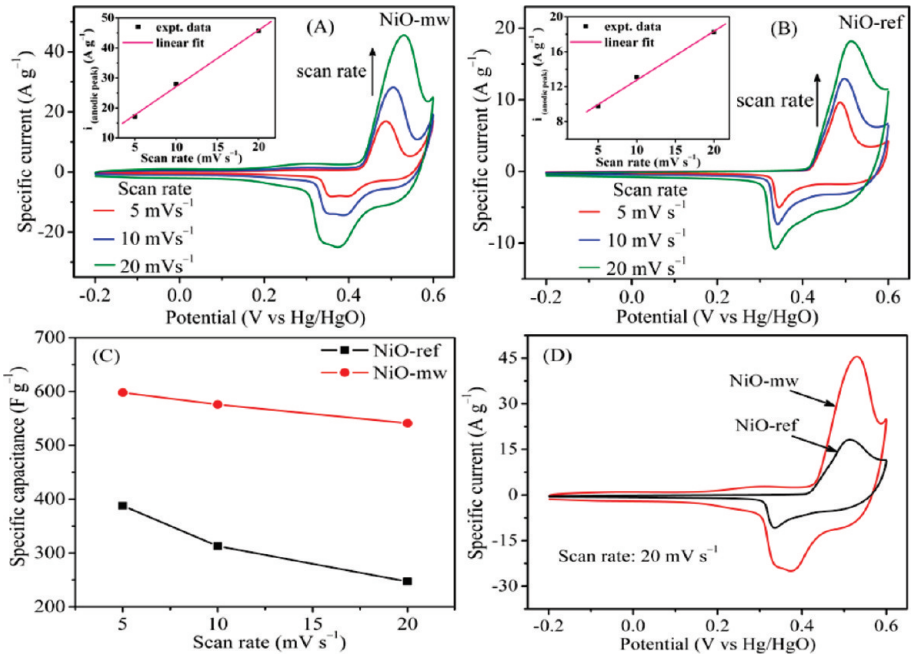

Figure 6. Cyclic voltammograms of (A) NiO-mw and (B) NiO-ref samples at different scan rates; (C) comparison of rate dependent specific capacitance values of NiO-mw and NiO-ref samples; and (D) comparison of cyclic voltammograms of NiO-mw and NiO-ref samples at a scan rate of 20 mv s^{-1}.

reported that that a pore size distribution in the range of 2−5 nm is favorable to improve the capacitance behavior of an electroactive material due to unhindered diffusion and accession of electrolyte ions into the inner space/matrix. In this context, the hierarchical porosity of NiO-ref and NiO-mw samples with maximum pore size distribution in the above specified range are supposed to facilitate better transportation of electrolyte through their nanochannels for efficient redox reactions during the charge storage process. Hence, the performance of these two NiO samples in electrochemical supercapacitor application has been studied by cyclic voltammetry (CV), galvanostatic charge−discharge (CP), and electrochemical impedance spectroscopy (EIS).

3.1. Electrochemical Study. The CV measurements on NiO-mw and NiO-ref electrodes are performed at sweep rates of 5, 10, and 20 mV s^{-1} in the potential range of −0.2 to 0.6 V (vs Hg/HgO) to evaluate the rate dependent supercapacitive performance of the samples. The CV patterns of NiO-mw and NiO-ref samples are shown in panels A and B in Figure 6, respectively. The NiO electrodes were initially stabilized for 25 CV cycles before the final measurements. The CV patterns of both the samples show identical shapes, which are typical of pseudocapacitance behavior due to occurrence of Faradaic redox reactions in the system. The respective anodic and cathodic peaks at the positive and negative current density correspond to following charge−discharge phenomena.[17−20]

$$\mathrm{NiO} + z\mathrm{OH}^- \underset{\text{discharge}}{\overset{\text{charge}}{\rightleftharpoons}} z\mathrm{NiOOH} + (1-z)\mathrm{NiO} + ze^- \qquad (1)$$

The oxidation and reduction peak potentials in the CV graphs are denoted as E_O and E_R respectively. The potential at which the oxygen-evolution reaction occurs is denoted as E_{OE}. The unsymmetrical nature in the redox peaks of the respective NiO samples indicates kinetic irreversibility in the redox process. This can be ascribed to ohmic resistance and polarization because of the electrolyte diffusion in the porous electrode during the redox reactions.[51] The smaller $E_O - E_R$ (ΔE) value is a measure of better reversibility in the redox reaction and from Figure 6D it is found that NiO-mw sample (ΔE = 158 mV) shows better reaction reversibility than NiO-ref sample (ΔE = 177 mV).[19] This is due to preferred rippled-shaped surface morphology of NiO-mw sample which promotes easy diffusion of OH^- ions for higher reversibility during the redox reactions.[52] From the insets of A and B in Figure 6, almost linear (quasi-linear) relationship has been observed between the anodic peak current density and the scan rate.[53] This again indicates the contribution of surface redox reactions in the pseudocapacitance behavior of the NiO electrodes. The specific capacitance (C_s, F g^{-1}) values at different scan rates (ν, V s^{-1}) in the CV measurements were calculated using the following equation:[17−19]

$$C_s = \frac{1}{\nu w(\Delta V)} \int_{Va}^{Vc} iVdV \qquad (2)$$

where ΔV (V) is the applied potential window (Va to Vc) and w (g) is the weight of the active material. The specific capacitance values of the samples are calculated by integration of potential versus specific capacitance graphs as shown in Figure S2 in the Supporting Information. The calculated specific capacitance values for NiO-mw at scan rates of 5, 10, and 20 mV s^{-1} are 598, 576, and 541 F g^{-1}, respectively. Similarly, the specific capacitance values for NiO-ref at the same scan rates are 388, 313, and 247 F g^{-1}, respectively. There is only 9.5% loss in specific capacitance value for NiO-mw sample at 20 mVs^{-1} as compared to 36.3% loss for NiO-ref sample (Figure 6C). This demonstrates higher current response of NiO-mw sample. The noticeable improvement in specific capacitance values of NiO-mw sample is due to the participation of rippled-shaped channels which assist

maximum contact with OH^- ions for redox reaction. It is known that at lower scan rates, both outer- and the inner-pore surfaces of the electrode materials are effectively utilized during OH^- ion propagation, whereas at high scan rates, mainly outer regions of the pores are accessed by the ions.[7,17,51,54] Therefore, although NiO-mw sample shows lower BET surface area and pore volume, the prefect rippled-shaped nanochannels assist higher surface accession of OH^- ions even at elevated scan rate, which results in better capacitance retention at higher redox reaction conditions (Scheme 2). The higher fraction of accessible Ni sites (z) at a fixed scan rate is also a signature of better performance of a NiO sample. The value of "z" in eq 1 has been estimated from the specific capacitance values of the NiO-mw and NiO-ref samples (from CV measurements) using the following expression[55]

$$z = \frac{CM\Delta V}{F} \tag{3}$$

where ΔV, M, F, and C correspond to the potential window (0.8 V), molecular weight of NiO (74.692 g), Faraday constant (96 487 C/equiv.) and specific capacitance values at scan rate of 20 mVs^{-1}, respectively. The respective "z" values of NiO-mw and NiO-ref samples are calculated to be 0.335 and 0.153. This reveals that significantly higher fractions (~34%) of Ni atoms of NiO-mw sample are accessible to the OH^- ions during the redox reactions as compared to the NiO-ref sample (~15%). This further corroborates that more Ni^{2+} sites of ripple-shaped porous surface gets electrochemically exposed to redox reactions than the flaky surface (Scheme 2).[52] These results clearly suggest the control of surface morphology of the electrode materials on their supercapacitor performance.

Scheme 2. Pictorial Representations of the Accessibility of OH^- Ions to (A) Rippled Surfaces (NiO-mw sample) and (B) Flakelike Surfaces ((NiO-ref sample)

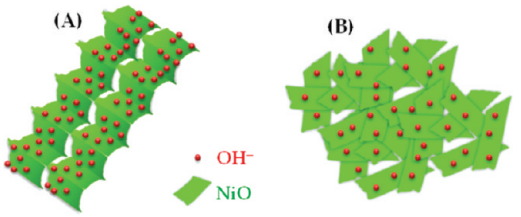

As cyclic performance and stability of an electrode material are very significant for its potential use in a supercapacitor device, the charge−discharge measurements were performed on both the NiO samples at different current densities. Figure 7A and 7B shows the respective discharge curves of NiO-mw and NiO-ref samples at current densities of 0.5, 1.0, 2.0, and 4.0 Ag^{-1}. All the nonlinear discharge curves, irrespective of the applied current density, are characteristics of pseudocapacitance behavior of the NiO samples due to electrochemical adsorption/desorption or quasi-reversible redox reactions at the electrode−electrolyte interface.[56] From panels A and B in Figure 7, it is clear that the NiO-mw sample exhibits longer discharge time than NiO-ref sample at the same current density, which signifies better charge storage performance of the NiO-mw sample. From the charge−discharge measurements at different current densities, the specific capacitance values of NiO samples have been calculated using applied charge or discharge current (i), mass of the NiO samples (m), discharge time (Δt) and applied potential (ΔV = 0.55 V) in the following equation[9,16,31]

$$C_s = \frac{i(\Delta t)}{m(\Delta V)} \tag{4}$$

The specific capacitance values of NiO-mw sample at scan rates of 0.5, 1.0, 2.0, and 4.0 A g^{-1} are found to be 420, 399, 372, and 337 F g^{-1}, respectively. Similarly, the specific capacitance values

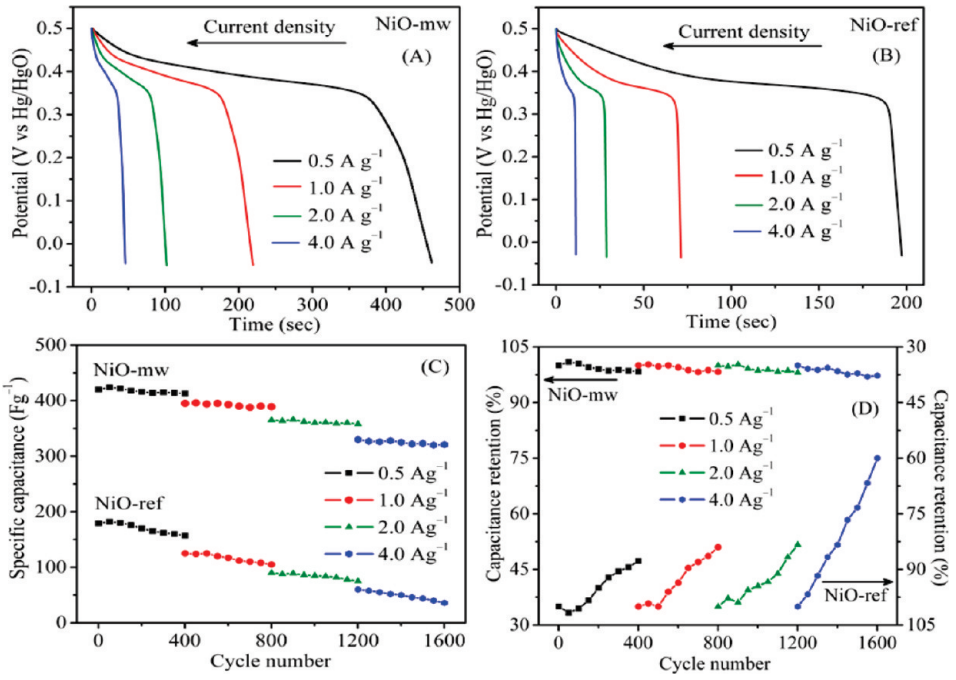

Figure 7. Discharge curve of (A) NiO-mw and (B) NiO-ref samples at different current densities; (C) comparison of current density dependent specific capacitance values of NiO-mw and NiO-ref samples with cycling; and (D) comparison of current density dependent specific capacitance retention of NiO-mw and NiO-ref samples with cycling.

for NiO-ref sample at the same scan rates are found to be 179, 130, 107, and 84 F g^{-1}, respectively. The decrease in specific capacitance values with increasing current density is significantly less for the NiO-mw sample than for the NiO-ref sample. This is an indication of the superior rate behavior of the NiO-mw sample as compared to the NiO-ref sample. This is due to the improved surface properties of NiO-mw sample. Because of the presence of numerous nanochannels, the rippled-shaped porous morphology acts as perfect "OH^- ion-buffering reservoir" and facilitates enhanced contact, diffusion as well as penetration of OH^- ions for faster electrode kinetics and maximum reversible redox processes for charge storage.[57] On the other hand, the flake structure of NiO-ref sample, although having higher surface area, is devoid of more electro-active surface sites and better electrolytic contact, which results in reduced charge storage capacity of the material.

As higher life-cycle stability is very crucial for an electrode material to be practically used in electrochemical capacitor, both the NiO samples were tested for 400 galvanostatic charge−discharge cycles at each current density of 0.5, 1.0, 2.0, and 4.0 A g^{-1}. Figure 7C shows the plots of estimated specific capacitance values of NiO-mw and NiO-ref samples versus charge−discharge cycles at different current densities. Figure 7D shows the plots of capacity retention (%) of the samples with charge−discharge cycles at different current densities. From the Figure 7C and 7D, it can be observed that NiO-mw sample shows significantly better capacitance retention and stability than NiO-ref sample. The capacitance retention of the NiO-mw sample after 400 charge discharge−discharge cycles at current densities of 0.5, 1.0, 2.0, and 4.0 A g^{-1} are found to be 98.35, 98.28, 98.08, and 97.27%, respectively. However, the capacitance retentions for NiO-ref sample at similar current density are 87.70, 84.0, 83.33, and 60.0% respectively. This is attributable to the network of rippled-shaped porous structure of NiO-mw sample which is better accessible to the OH^- ions even at higher current density conditions. The negligible decrease in specific capacitance value of the NiO-mw material at higher current density condition during long cycling is also due to the insignificant structural/crystallographic modification or degradation of the electro-active surface through the recurring insertion/extraction of OH^- ions. However, the flaky NiO-ref sample although possess higher surface area, the OH^- ions cannot fully access the electro-active surface due to its unsuitable surface morphology and porosity. At higher current density conditions, the flake structure also suffers considerable degradation which further restricts the occurrence of sufficient number of redox reactions. Therefore, at higher current density condition for longer time, drastic decrease in the specific capacitance value and cyclic stability is observed for flaky NiO-ref sample. Small increase in specific capacitance values for initial 10−12 charge−discharge cycles is observed for both the samples at different current density, which is ascribed to the surface activation (pore opening) of the porous structures. The charging and discharging curves of the samples (see Figures S3 and S4 in the Supporting Information) at all current densities are not completely symmetrical for both the samples which are related to some kinetic irreversibility of the OH^- ions on the porous NiO surface during redox reactions.[19,58] This can be substantiated from the $\Delta t = (t_C - t_D)$ value, where t_C and t_D are the charging and discharging times, respectively. The smaller Δt value for NiO-mw sample due to easy accessibility of OH^- ions shows the higher redox reversibility than the NiO-ref sample. The Coulombic efficiency "η", a measure of competence of charge transfer in an electrochemical reaction, is calculated from the charge−discharge cycles of NiO-mw and NiO-ref samples. During the cyclic study, the Coulombic efficiency of NiO-mw sample for the first charge−discharge cycles at current density of 0.5, 1.0, 2.0, and 4.0 A g^{-1} are found to be 92.3, 95.2, 101.3, and 100.98%, respectively (Figure 8).

The "η" values for the NiO-mw sample almost reaches ~100% during charge−discharge cycles at different current densities. This suggests higher feasibility of the redox process even at higher current density condition. The pronounced increase in "η" value of NiO-mw sample is a characteristics of increase in kinetic reversibility with cycling. However, the lower and decreasing "η" value of NiO-ref sample during cycling at similar current density operation conditions supports the poor accessibility

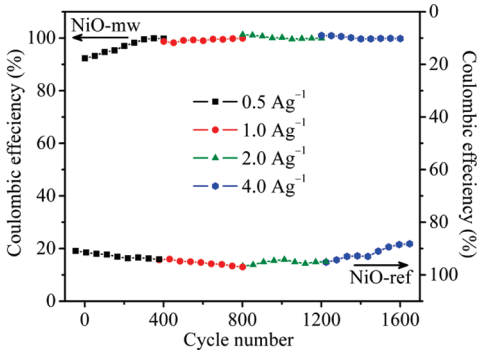

Figure 8. Coulombic efficiency (η) of NiO-mw and NiO-mw samples, calculated from charge−discharge cycles at different current densities.

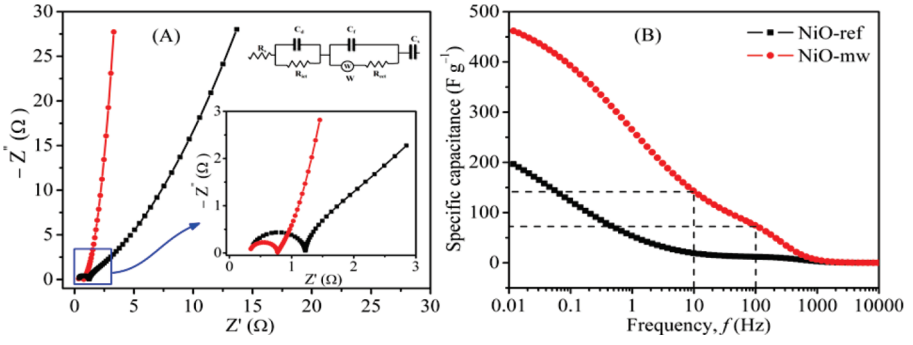

Figure 9. (A) Complex plane impedance plots (Nyquist plots) of NiO-mw and NiO-ref samples; Insets show the equivalent circuit and impedance at high frequency region; (B) Frequency dependent specific capacitance values of NiO-mw and NiO-ref samples, calculated from impedance measurements.

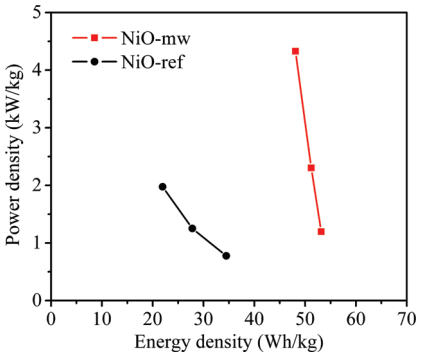

Figure 10. Ragone plots (power density versus energy density) of NiO-mw and NiO-ref samples. The values are derived from CVs at various scan rates.

of OH^- ions into the flaky structure at higher current density. The microwave synthesized rippled-shaped porous NiO sample is therefore electrochemically preferred for electrochemical supercapacitor application than the reflux synthesized flaky NiO material.

As lower electronic resistance (higher electronic conductivity) is a significant property of an electroactive material to be used in supercapacitors, both the NiO samples were subjected to AC impedance measurements between 0.01 and 1×10^5 Hz to quantitatively evaluate their intrinsic resistance and relative capacitive performance. Figure 9A shows the complex-plane impedance plots (imaginary part, Z'' versus real part, Z') of the NiO electrodes with potential amplitude of 0.5 V. The impedance data plots were fitted (CNLS fitting method) to a Randle equivalent circuit (inset in Figure 9A).[59] The different parameters in the equivalent circuit are characteristic of various electrochemical processes in the electrode−electrolyte interface at the specific operating frequency range. As the surface structures of both the NiO samples are fairly different, the obvious dissimilarity in charge propagation phenomena during the Faradaic redox reactions is reflected as two partial semicircles in the high and medium frequency regions. The enlarged view of the higher frequency semicircles is shown as the inset in Figure 9A. This is the characteristic of the processes occurring at the oxide−electrolyte interface which has been modeled as a double-layer capacitor, C_d, in parallel with a charge−transfer resistor, R_{ict}. The R_{ict} arises from the discontinuity in the charge transfer process at the electrode−electrolyte interface due to the conductivity difference between the solid oxide (electronic conductivity) and liquid electrolyte phase (ionic conductivity). From Figure 9A, it is seen that R_{ict} value of NiO-mw sample is lower than that of the NiO-ref sample which can be attributed to the unique surface morphology and higher electro-active surface area of NiO-mw sample. The impedance behavior of the NiO samples at the medium frequency regions is characteristic of surface redox reaction induced charge-transfer resistance. This phenomenon can be represented as a combination of film capacitor, C_f, in parallel with an electron-transfer resistor, R_{ect}. The EIS plots of the NiO samples in the lower frequency region are nearly linear which are typical of Warburg impedance, W. The resistance in these regions is attributed to diffusion of the OH^- ions within the pores of NiO electrode during redox reactions. The distinctive near-straight vertical line of NiO-mw sample as compared to NiO-ref sample demonstrates lower diffusion resistance due to easy access of the OH^- ions into the rippled-shaped porous structure during charge storage. By and large, the AC impedance measurements substantiate the lower resistance (lower equivalent series resistance, ESR) of NiO-mw sample which is the combination of ionic resistance of electrolyte, intrinsic resistance of active materials and contact resistance at the active material/current collector interface. The specific capacitance (C_s) values of both the NiO electrodes were calculated from the impedance data, using the following equation[5,7,17−19]

$$C_s = \frac{1}{2\pi f Z''} \tag{5}$$

The frequency-dependent specific capacitance calculated from impedance analysis is shown in Figure 9B. The specific capacitance values of NiO-mw sample are found to be significantly higher than the NiO-ref sample in the entire frequency range. Moreover, the appreciably higher specific capacitance values of NiO-mw sample at elevated operating frequency (142 F g^{-1} at 10 Hz and 73 F g^{-1} at 100 Hz) demonstrate the high power performance and excellent rate response of the sample. The NiO-ref sample, in contrast, shows poor power performance and rate response due to the lesser structural and electrochemical stability of flaky structure at higher frequency. The better power performance of the NiO-mw sample over NiO-ref sample has been further verified from the Ragone plot (power density versus energy density) in Figure 10. The energy and power densities were derived from CV analysis at the scan rates of 5, 10, and 20 mV s^{-1}. The energy density values (d_E) were obtained using the equation[60,61]

$$d_E = \frac{1}{2} CV^2 \tag{6}$$

where "C" is the specific capacitance (F g^{-1}) at a particular scan rate within the potential window (V) of 0.8 V. The power density values (d_P) were obtained by dividing the "d_E" with time "t" for one sweep segment at a fixed scan rate.

$$d_P = \frac{d_E}{t} \tag{7}$$

There is considerable improvement in energy and power density of NiO-mw sample over NiO-ref sample. It shows that NiO-mw is more suitable to supercapacitor applications. All together, the detailed physicochemical and electrochemical experiments established that the NiO-mw material designed by microwave synthesis has significant advantage over the NiO-ref sample obtained by conventional-reflux method. This has been possible because NiO-mw sample allows its inner surface through the rippled-shaped porous structure to accessed by the OH^- ions rather freely.

This study reveals the importance of microwave-mediated synthesis to prepare porous NiO in a nonhydrothermal homogeneous precipitation method which is found to have significant advantage over conventional-reflux method in producing samples with added uniform surface structure and superior surface properties for enhanced supercapacitor performance. This approach, we believe, will promote the future development of electrode materials based on NiO for fabricating wide range of electrochemical supercapacitor devices.

4. CONCLUSION

In the present work, we have demonstrated the nonhydrothermal synthesis of hierarchically porous NiO samples by adopting

conventional-reflux and microwave assisted reflux methods. The synthesis methods are found to have significant influence on the surface morphology and porosity of the NiO material. Electrochemical studies show that there is an explicit contribution of pseudocapacitance to the energy storage performance of the NiO materials. The cyclic voltammetry study shows considerably improved high rate pseudocapacitance of the NiO-mw sample due to facile electrolyte penetration and better Faradaic utilization of the electro-active rippled-shaped porous surface. The charge−discharge study shows that the NiO-mw sample exhibits superior high rate pseudocapacitance behavior, cyclic stability and Coulombic efficiency over the NiO-ref sample under different current density operation conditions. This is due to better electrochemical accessibility of OH^- ions to rippled surface than smooth flaky surface even at higher current density conditions. The impedance analysis shows the contribution of redox process to the charge storage mechanism and NiO-mw is found to possess lower ESR value than the NiO-ref sample. Again the NiO-mw sample is demonstrated to be a better material for higher frequency pseudocapacitor application. It is further established from the Ragone plot that the microwave synthesized NiO-mw sample has higher energy and power densities than the reflux synthesized NiO-ref sample. This simple strategy to synthesize NiO with novel morphology and superior electrode properties makes it a prospective method to fabricate other electro-active materials.

■ ASSOCIATED CONTENT

Supporting Information. SEM of uncalcined precursors, scan rate versus specific capacitance graphs from CV, and initial charge−discharge cycles of NiO samples at different current densities. This material is available free of charge via the Internet at http://pubs.acs.org.

■ AUTHOR INFORMATION

Corresponding Author

*E-mail: grrao@iitm.ac.in. Tel.: (91) 44 2257 4226. Fax.: (91) 44 2257 4202.

■ ACKNOWLEDGMENT

Financial support from DRDO, New Delhi, through Grant ERIP/ER/0600319/M/01/1052 is gratefully acknowledged. We thank SERC division of DST, Ministry of Science and Technology, New Delhi, for providing powder XRD, TGA, and BET facilities (under FIST Schemes), and MNRE, New Delhi, for providing CHI 7081C electrochemical workstation for electrochemical measurements. We thank Mr. A. Narayanan and Mrs. S. Srividya for TGA, BET, and XRD data collection.

■ REFERENCES

(1) Hall, P. J.; Mirzaeian, M.; Fletcher, S. I.; Sillars, F. B.; Rennie, A. J. R.; Shitta-Bey, G. O.; Wilson, G.; Andrew, C.; Carter, R. *Energy Environ. Sci.* **2010**, *3*, 1238–1251.

(2) Shukla, A. K.; Sampath, S.; Vijayamohanan, K. *Curr. Sci.* **2000**, *79*, 1656–1661.

(3) Winter, M.; Brodd, R. J. *Chem. Rev.* **2004**, *104*, 4245–4269.

(4) Aricò, A. S.; Bruce, P.; Scrosati, B.; Tarascon, J. M.; Schalkwijk, W. *Nat. Mater.* **2005**, *4*, 366–377.

(5) Kötz, R.; Carlen, M. *Electrochim. Acta* **2000**, *45*, 2483–2498.

(6) Simon, P.; Gogotsi, Y. *Nat. Mater.* **2008**, *7*, 845–854.

(7) Conway, B. E. *Electrochemical Supercapacitors: Scientific Fundamentals and Technological Applications*; Kluwer Acdemic/Plenum: New York, 1999.

(8) Burke, A. *Electrochim. Acta* **2007**, *53*, 1083–1091.

(9) Conway, B. E.; Birss, V.; Wojtowicz, J. *J. Power Sources* **1997**, *66*, 1–14.

(10) Jayalakshmi, M.; Balasubramanian, K. *Int. J. Electrochem. Sci.* **2008**, *3*, 1196–1217.

(11) (a) Zhang, Y.; Feng, H.; Wu, X.; Wang, L.; Zhang, A.; Xia, T.; Dong, H.; Li, X.; Zhang, L. *Int. J. Hydrogen Energy* **2009**, *34*, 4889–4899. (b) Biswas, S.; Drzal, L. T. *ACS Appl. Mater. Interfaces* **2010**, *2*, 2293–2300.

(12) Hu, C.-C.; Chang, K.-H.; Lin, M.-C.; Wu, Y.-T. *Nano Lett.* **2006**, *6*, 2690–2695.

(13) Naoi, K.; Simon, P. *The Electrochem. Soc. Interface* **2008**, 34–37.

(14) Bélanger, D.; Brousse, T.; Long, J. W. *The Electrochem. Soc. Interface* **2008**, 49–52.

(15) Ragupathy, P.; Park, D. H.; Campet, G.; Vasan, H. N.; Hwang, S.-J.; Choy, J.-H.; Munichandraiah, N. *J. Phys. Chem. C* **2009**, *113*, 6303–6309.

(16) Zhang, X.; Shi, W.; Zhu, J.; Zhao, W.; Ma, J.; Mhaisalkar, S.; Maria, T. L.; Yang, Y.; Zhang, H.; Hng, H. H.; Yan, Q. *Nano Res.* **2010**, *3*, 643–652.

(17) Meher, S. K.; Justin, P.; Ranga Rao, G. *Electrochim. Acta* **2010**, *55*, 8388–8396.

(18) Justin, P.; Meher, S. K.; Ranga Rao, G. *J. Phys. Chem. C* **2010**, *114*, 5203–5210.

(19) Meher, S. K.; Justin, P.; Ranga Rao, G. *Nanoscale* **2011**, *3*, 683–692.

(20) (a) Yuan, C.; Zhang, X.; Su, L.; Gao, B.; Shen, L. *J. Mater. Chem.* **2009**, *19*, 5772–5777. (b) Juodkazis, K.; Juodkazytė, J.; Vilkauskaitė, R.; Jasulaitienė, V. *J. Solid State Electrochem.* **2008**, *12*, 1469–1479.

(21) Zhu, T.; Chen, J. S.; Lou, X. W. *J. Mater. Chem.* **2010**, *20*, 7015–7020.

(22) Brezesinski, T.; Wang, J.; Tolbert, S. H.; Dunn, B. *Nat. Mater.* **2010**, *9*, 146–151.

(23) Wee, G.; Soh, H. Z.; Yan, C. L.; Mhaisalkar, S. G.; Srinivasan, M. *J. Mater. Chem.* **2010**, *20*, 6720–6725.

(24) Dong, S.; Chen, X.; Gu, L.; Zhou, X.; Xu, H.; Wang, H.; Liu, Z.; Han, P.; Yao, J.; Wang, L.; Cui, G.; Chen, L. *ACS Appl. Mater. Interfaces* **2011**, *3*, 93–98.

(25) Lang, J.-W.; Kong, L.-B.; Wu, W.-J.; Luo, Y.-C.; Kang, L. *Chem. Commun.* **2008**, 4213–4215.

(26) Pang, H.; Lu, Q.; Zhang, Y.; Lia, Y.; Gao, F. *Nanoscale* **2010**, *2*, 920–922.

(27) Liu, K.-C.; Anderson, M. A. *J. Electrochem. Soc.* **1996**, *143*, 124–130.

(28) Yu, C.; Zhang, L.; Shi, J.; Zhao, J.; Gao, J.; Yan, D. *Adv. Funct. Mater.* **2008**, *18*, 1544–1554.

(29) Zhou, W.; Yao, M.; Guo, L.; Li, Y.; Li, J.; Yang, S. *J. Am. Chem. Soc.* **2009**, *131*, 2959–2964.

(30) Nam, K.-W.; Kim, K.-B. *J. Electrochem. Soc.* **2002**, *149*, A346–A354.

(31) Xia, X.; Tu, J.; Wang, X.; Gu, C.; Zhao, X. *J. Mater. Chem.* **2011**, *21*, 671–679.

(32) Yuan, C.; Xiong, S.; Zhang, X.; Shen, L.; Zhang, F.; Gao, B.; Su, L. *Nano Res.* **2009**, *2*, 722–732.

(33) Bilecka, I.; Niederberger, M. *Nanoscale* **2010**, *2*, 1358–1374.

(34) Tompsett, G. A.; Conner, W. C.; Yngvesson, K. S. *Chem. Phys. Chem.* **2006**, *7*, 296–319.

(35) Jhung, S. H.; Jin, T.; Hwang, Y. K.; Chang, J.-S. *Chem. Eur. J.* **2007**, *13*, 4410–4417.

(36) Polshettiwar, V.; Baruwati, B.; Varma, R. S. *ACS Nano* **2009**, *3*, 728–736.

(37) Song, X.; Gao, L. *J. Am. Ceram. Soc.* **2008**, *91*, 3465–3468.

(38) Xu, L.; Ding, Y.-S.; Chen, C.-H.; Zhao, L.; Rimkus, C.; Joesten, R.; Suib, S. L. *Chem. Mater.* **2008**, *20*, 308–316.

(39) Soler-Illia, G. J. A. A.; Jobbgy, M.; Regazzoni, A. E.; Blesa, M. A. *Chem. Mater.* **1999**, *11*, 3140–3146.

(40) Hu, X.; Gong, J.; Zhang, L.; Yu, J. C. *Adv. Mater.* **2008**, *20*, 4845–4850.
(41) Patzke, G. R.; Zhou, Y.; Kontic, R.; Conrad, F. *Angew. Chem., Int. Ed.* **2011**, *50*, 826–859.
(42) Cölfen, H.; Antonietti, M. *Angew. Chem., Int. Ed.* **2005**, *44*, 5576–5591.
(43) Whitesides, G. M.; Boncheva, M. *Proc. Natl. Acad. Sci. U.S.A.* **2002**, *99*, 4769–4774.
(44) Banfield, J. F.; Welch, S. A.; Zhang, H.; Ebert, T. T.; Penn, R. L. *Science* **2000**, *289*, 751–754.
(45) (a) Bromley, S. T.; Moreira, I. P. R.; Neyman, K. M.; Illas, F. *Chem. Soc. Rev.* **2009**, *38*, 2657–2670. (b) Meldrum, F. C.; Cölfen, H. *Chem. Rev.* **2008**, *108*, 4332–4432. (c) Klimakow, M.; Leiterer, J.; Kneipp, J.; Rössler, E.; Panne, U.; Rademann, K.; Emmerling, F. *Langmuir* **2010**, *26*, 11233–11237.
(46) Song, R.-Q.; Cölfen, H. *Adv. Mater.* **2010**, *22*, 1301–1330.
(47) Zheng, J.; Yang, R.; Xie, L.; Qu, J.; Liu, Y.; Li, X. *Adv. Mater.* **2010**, *22*, 1451–1473.
(48) Zheng, Y.; Ding, H.; Zhang, M. *Mater. Res. Bull.* **2009**, *44*, 403–407.
(49) Rouquerol, F.; Rouquerol, J.; Sing, K. *Adsorption by Powders and Porous Solids*; Academic Press: London, 1999.
(50) Rose, M.; Böhlmann, W.; Sabo, M.; Kaskel, S. *Chem. Commun.* **2008**, 2462–2464.
(51) Pell, W. G.; Conway, B. E. *J. Electroanal. Chem.* **2001**, *500*, 121–133.
(52) Zheng, F.-L.; Li, G.-R.; Ou, Y.-N.; Wang, Z.-L.; Su, C.-Y.; Tong, Y.-X. *Chem. Commun.* **2010**, *46*, 5021–5023.
(53) Hu, C.-C.; Wang, C.-C.; Chang, K.-H. *Electrochim. Acta* **2007**, *52*, 2691–2700.
(54) Pell, W. G.; Conway, B. E.; Marincic, N. *J. Electroanal. Chem.* **2000**, *491*, 9–21.
(55) Srinivasan, V.; Weidner, J. W. *J. Electrochem. Soc.* **2000**, *147*, 880–885.
(56) Zhao, D.-D.; Bao, S.-J.; Zhou, W.-J.; Li, H.-L. *Electrochem. Commun.* **2007**, *9*, 869–874.
(57) Wang, D.-W.; Li, F.; Liu, M.; Lu, G. Q.; Cheng, H.-M. *Angew. Chem., Int. Ed.* **2008**, *47*, 373–376.
(58) Conway, B. E. *J. Electrochem. Soc.* **1991**, *138*, 1539–1548.
(59) Hu, C.-C.; Chang, K.-H.; Tung, Y. H. *J. Electrochem. Soc.* **2008**, *155*, F196–F200.
(60) Jang, J. H.; Kato, A.; Machida, K.; Naoi, K. *J. Electrochem. Soc.* **2006**, *153*, A321–A328.
(61) Wang, H.; Casalongue, H. S.; Liang, Y.; Dai, H. *J. Am. Chem. Soc.* **2010**, *132*, 7472–7477.